Study of ice accretion on wind turbine blade profiles using thermal infrared imaging

Adeel Yousuf (iD), Jia Yi Jin, Pavlo Sokolov and Muhammad S Virk

Abstract

Atmospheric icing has been recognized as hindrance in proper utilization of good wind resources in cold regions. There is a growing need to better understand the ice accretion physics along wind turbine blades to improve its performance and for optimal design of anti/de-icing system. This article describes a study of ice accretion along wind turbine blade profiles using thermal infrared imaging. Surface temperature distribution along four different blade profile surfaces is studied at different operating conditions. Analysis shows that surface temperature distribution along blade profile surface during ice accretion process is a dynamic process and change in atmospheric conditions and blade geometric characteristics significantly affects the surface temperature and resultant ice accretion. The effect of blade geometry on ice accretion is more prominent in case of wet ice conditions due to low freezing fraction and water run back along blade profile surface.

Keywords

Wind turbine, atmospheric icing, thermal infrared image, icing tunnel, blade profile

Introduction

Human activities are increasingly extending in the high north regions, where atmospheric icing not only creates human inconvenience but can also affect human industrial activities, while it accretes on various structure. Atmospheric icing on structures is a key factor when planning infrastructures in cold regions due to its huge economic consequences. Structures are not passive during ice accretion, but can experience devastating forces to which they respond. Better understanding of ice accretion physics has gotten attention several decades before mainly due to ice accretion on aircrafts, as it can pose a serious flight danger (Hudecz, 2014). Similarly, in recent years due to increased energy demands in high north, icing on wind turbine blades has got attention as it affects blade aerodynamics that lead to decrease in annual power production and can pose a safety risk due to ice shedding (Tammelin et al., 2000). Atmospheric ice accretion on wind turbine mainly occurs due to the impingement of super-cooled water droplets that freeze on blade surface (Afzal and Virk, 2018). The distribution of ice loads along blade surface is not constant due to change in airflow behaviour and geometric characteristics of the blade from root to tIp section. For better understanding of wind turbine performance in icing conditions, it is important to study the ice accretion physics along wind turbine blade surface. Understanding of airflow and droplet behaviour with surface temperature distribution along blade surface during ice accretion is important to get a better insight. Study of ice accretion physics along wind turbine blade has been carried out by various researchers using analytical, numerical and experimental techniques. Blade surface temperature during ice accretion is a dynamic parameter. A good understanding of the blade surface temperature distribution can give a better insight of ice accretion physics. Infrared (IR) imaging thermometry technique can be utilized to quantitatively measure the variations of

Arctic Technology & Icing Research Group, Faculty of Engineering Science and Technology, UiT-The Arctic University of Norway, Narvik, Norway

Corresponding author:
Adeel Yousuf, Arctic Technology & Icing Research Group, Faculty of Engineering Science & Technology, UiT-The Arctic University of Norway, Lodve Langesgate 2, 8515 Narvik, Nordland, Norway.
Email: ayo005@post.uit.no

temperature distributions on blade surface to better understand the underlying physics of wind turbine blades icing (Guo et al., 2017).

Thermal infrared ice detection works on the principle that any surface or body that has a temperature above $0K$ emits thermal radiation depending upon its surface emissivity. Thermal signature can be sensed by a receiver such as thermal camera, which may be either active or passive. Active imaging techniques use artificial IR lighting source to illuminate the target image in which there may be icing present; then an infrared sensor collects the reflecting signal. A plethora of successive images over a number of sub-bands are collected, which are then processed to determine whether ice is present and, furthermore, to compute ice thickness using computational algorithms. One example of the active method is the 'Ice Camera' which has been developed by MacDonald, Dettwiler and Associates Ltd. (MDA) in a joint research project between US Army and NASA (Meitzler et al., 2007). Gong and Bansmer (2015) presented a Mid-Infrared (MIR) Laser scanning to trace the 3-D shape evolution of the ice growth without any interruption in the icing process. They produced their results using NACA 0012 airfoil. Rashid et al. (2019) used IR thermography equipment to measure marine ice thickness and established a correlation between time to respond (initial temperature) and icing thickness. Light et al. (2012) used data received from thermal imaging cameras equipped with infrared micro-bolometer sensors at remote geographic sites (lakes and rivers) to determine icing events in real-time using image processing algorithms. Liu and Hu (2018) studied the effect of dry-ice and wet ice with thermal IR camera in an Icing Research Tunnel (IRT) for NACA0012 airfoil and deduced unsteady heat transfer equation in terms of convective heat transfer coefficient, impinging velocity and LWC for both the cases as a part of theoretical model. Gao et al. (2019) used thermal imaging on glaze ice covered wind turbine blade DU91-W2250 for active pitch control de-icing technology at different angles of attack with constant air-temp (–5°C), airstream velocity and LWC. They deduced that an increase in angle of attack (AoA) leads to an increase in ice accretion on pressure side but decrease at suction side.

This article presents an icing tunnel based experimental study of the surface temperature distribution and resultant ice accretion along wind turbine blade profile sections. The study is carried out at icing tunnel laboratory of Cranfield University, UK, by using thermal infrared image processing to measure surface temperature distribution during ice accretion along four different wind turbine blade profiles (S819, S826, S832, DU-W-180) at dry and wet ice conditions. DU96 W-180 is the low-speed airfoil with a thickness-to-length ratio of 0.18 and is widely used for tip section of large wind turbine blades due to high lift-to-drag ratio, insensitivity to roughness and low noise. S819 is a thick family airfoil and is used for 10 to 20 metre long stall-regulated wind turbine blades. S826 is designed for mid-scale size wind turbine with variable speed and pitch. It is normally used at blade tip section because of high lift, low-drag and insensitivity to roughness. S832 is a thick airfoil designed for blade tip section of wind turbine blade. In this research work, ice accretion during icing tunnel tests has been studied using video recording and IR thermal imaging at different operating conditions.

Experimental setup

Figure 1 shows the schematic overview of the experimental setup used in this study, carried out at the icing tunnel laboratory of Cranfield University (CU), UK. Four different wind turbine blade profiles (Figure 2, *listed in*Table 1) are used. Each profile has different geometric and aerodynamic features and is suitable for wind turbine blades. The surfaces of these profiles are made of galvanized steel (VGAL.V.D $\times$ SID $+$ Z275) with average surface roughness of 1 microns. Icing wind tunnel facility at CU has test section size (761 $\times$ 761 mm) and can create realistic icing conditions for medium volume diameter (MVD) ranging from 15 to 80 μm, liquid water content (LWC) from 0.05 to 3 g/m^3 and air temperature from –30°C to 30°C.

To closely monitor the ice accretion along each profile, three high-definition (HD) cameras were used for video recording and pictures during ice accretion process. One long wavelength (17 microns) thermal IR camera (FLIR A615) was used. Seven different experiments are carried out at fixed Reynolds number $= 3 \times 10^6$ for both dry (rime) and wet (glaze) ice conditions. Table 1 presents the operating conditions used for this experimental study.

Results and analysis

This section presents the results from each test case specified in Table 1. Analysis shows that ice mainly accreted along leading edge and its growth extended along blade profiles chord depending on geometric characteristics of each profile. Real-time imaging from three HD cameras is recorded during each test. For thermal IR imaging FLIR-A615 camera is used. These thermal images are analysed using image processing software (*IR Control*
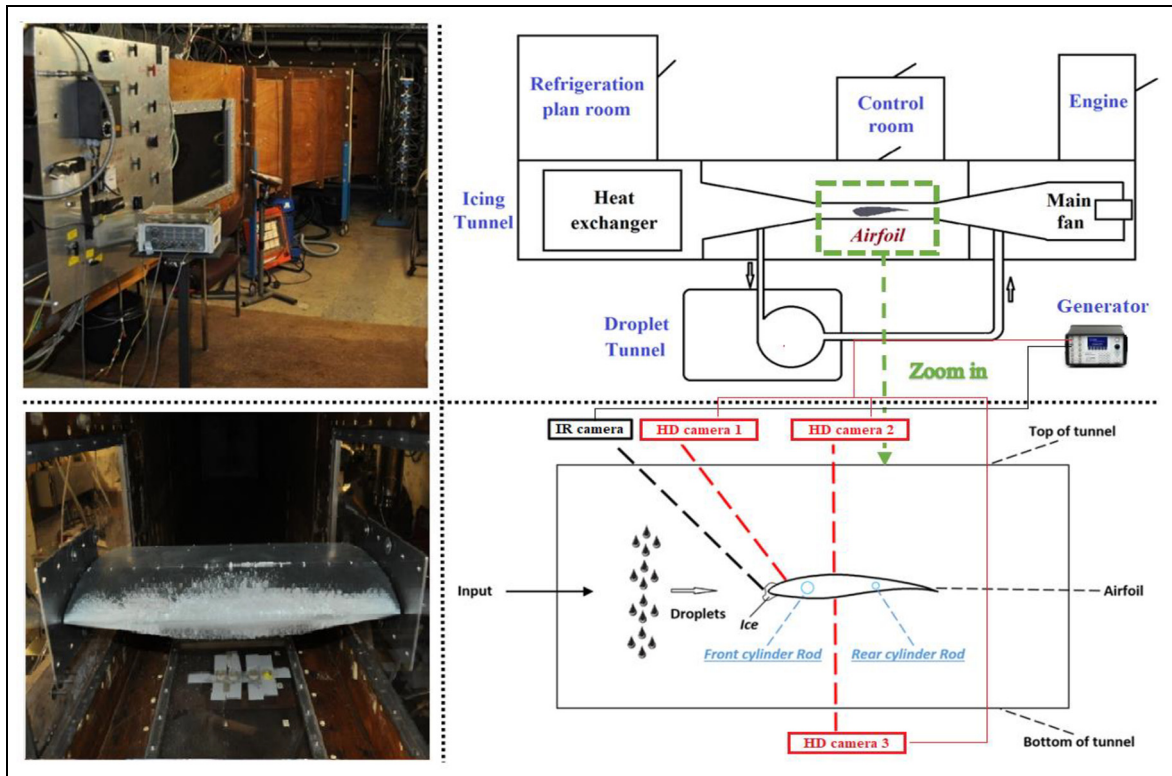
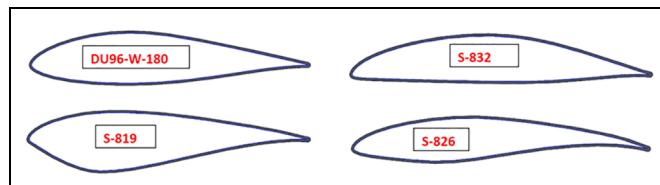**Figure 1.** Schematic view of the icing tunnel experimental setup.

Figure 2. Wind turbine blade profiles used in this study (cross-sectional view).

Table 1. Operating conditions for icing tunnel experiments.

Blade profile	Test	Ice type	Air velocity (m/s)	Temp (°C)	LWC (g/m³)	MVD (μm)	AOA (deg)	Icing duration (min)
DU96	1	Wet	77	−5	0.3	20	7	15
	2						0	
	3				1.6			
	4	Dry	70	−20	0.3			
S819	5	Wet	77	−5	0.5		0	
S826	6	Wet	77	−5	0.3		0	
S832	7	Dry	70	−20	0.3		0	

LWC: liquid water content; MVD: medium volume diameter; AOA: angle of attack.

v4.59), which provides the functionality to perform statistical operations at particular Areas of Interest (AOI). The captured infrared images are uploaded automatically to the computer through a USB type data logger and a signal-processing unit. The IR images are processed to detect ice by evaluating each profile surface temperature, which helped in identifying the ice distribution patterns and locations along each profile surface. In previous study
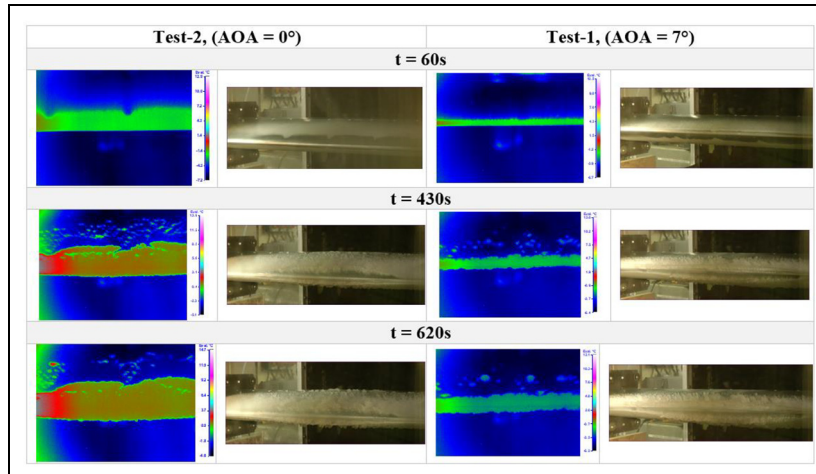
Figure 3. Area of interest (AOI).

Figure 4. Effect of AOA on ice accretion.

(Afzal and Virk, 2018; Ghani and Virk, 2013; Hudecz, 2014; Mohseni et al., 2012), results show that ice mainly accretes along leading edge, therefore, five different locations (as line) are marked along leading edge area of each profile during image processing for analysis of surface temperature variation. These locations are shown in Figure 3. For each test case, location # 1 and 2 correspond to pressure side of the blade profile, location # 3 corresponds to the leading edge at stagnation point and location # 4 and 5 correspond to the suction side of the profile. Surface temperature data obtained from image processing is imported to MATLAB for further analysis. During these analyses, the results are categorized with a focus on effect of:

- Angle of attack
- Liquid water content
- Wet/dry icing
- Airfoil geometry

In results section, plots are annotated with *test-a, test-b, test-c* and *test-d*, which are meant to mark the end of a dataset generated by IR Control software for single set of readings. HD camera recordings are synchronized with images of IR camera.

Effect of AoA

To study the effect of blade profile AoA on ice accretion, analyses are carried out using DU96 profile at two different AOA = 0° and 7° (*test case 1 & 2*). For test-2, along the stagnation line, clear and smooth wet glaze ice is formed (Figure 4). Horned ice structure at the centre of the blade profile perpendicular to the stagnation line appears with time. On the pressure side, wet glaze ice is accreted up to 25% of the chord length. Second impingement area lies on the back of the profile section (trailing edge) at about 85%–95% of the chord length, as a possible combination of runback water droplets and flow separation. Surface temperature profiles identify that ice
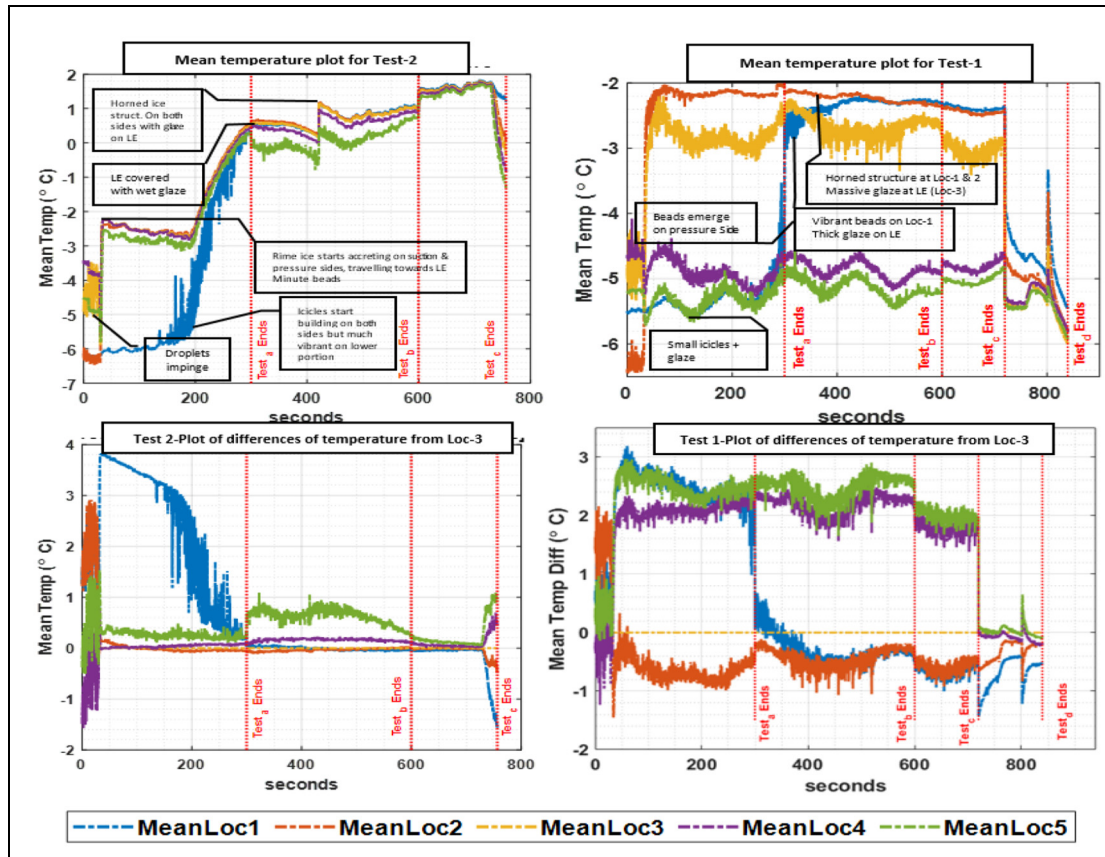
Figure 5. Surface temperature variations during ice accretion – AOA case.

starts to build up on the leading edge first and then along the pressure side. On the suction side (location 4, 5), change in temperature is almost negligible. For test-1, large, unconnected feathers of glaze ice with slight back-bow curvature extend up to 5%–7% of the chord length along suction side.

Analysis of AOA effect study shows an enlargement of accreted ice area around leading edge. At t = 60 s, this phenomenon is observed clearly when higher temperature occurs near the leading edge in both test cases due to high droplet impingement and freezing rate. IR image shows a nonlinear temperature gradient along the blade profile. Figure 5 shows the variation of surface temperature at 5 AOI locations along the profile surface as a function of droplet spray and icing time. Analyses show that icing beads formation at AOA = 0° takes place at about – 2.4°C (Figure 5 *top left image – see label at 40s*), whereas beads appear in case of AOA = 7° at same temperature range, but at a delayed time (*at ~290s for lower side and at ~325s for upper surface*). During the initial 30s (*for both cases*), all AOIs are at slightly different temperatures depending upon the surface emissivity. During icing process, water droplets mainly collide with the blade surface near leading edge (LE), and latent heat is released followed by the formation of an ice layer which forms due to partial or entire freezing of water droplets. Gao et al. (2017) suggests the succeeding process by the presence of water layer above frozen ice making two interfaces: blade–ice interface and ice–water interface (for both suction and pressure sides). They also explain the sudden rise in temperature due to the accumulation of bulge of ice at that AOI and increasing the AOA shifts the location of peaks. This is the same shift in peak as discussed previously for beads formation. With the change in AoA the airflow behaviour and location of super-cooled droplet impingement along blade surface changed, which led to change in blade surface temperature and resultant ice accretion.

Effect of LWC

To study the effect of LWC on blade surface temperature distribution during ice accretion (*Test 2 and 3*), analyses are carried our using DU96 profile. Two different LWC (0.3 gm^{-3} & 1.6 gm^{-3}) are used. For test-2, a relatively
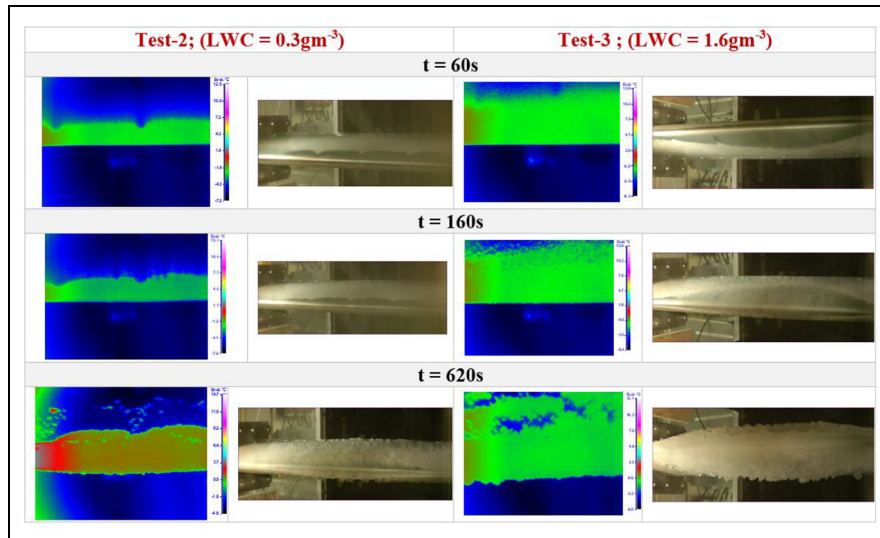
Figure 6. Effect of LWC on ice accretion.

smooth, clear glaze ice is formed at the LE, which extended almost equally (*10% of the chord length*) on both top and bottom surfaces of the profile. For test-3, wet ice with fine granules (rime ice) first appears on both suction and pressure side past the LE and then the transparent, horned ice structure appears equally on upper and lower surfaces of the profile. The results closely relate with Gao et al. (2019) with LWC = 1.1 gm^{-3}, though their wet operating conditions differ a bit in temperature and wind velocity.

Notable IR frames at three selective time instants as retrieved from IR Control software are shown in Figure 6. Temperature profiles for both the tests resemble each other except for the timing of mixed ice formation; mixed ice starts forming earlier in high LWC than in low LWC (*beads can be observed at t* = 160 s). Initially rime ice builds up on both suction and pressure sides. Moreover, high LWC targets the LE. One clear visual difference as depicted in both infrared and HD images is thickness of ice. Figure 7 shows the temperature curves and temperature difference curves (*w.r.t. LE temp*). Graphics of Test-2 are the same as previous and a close-up suggests that enhancing the LWC to 1.6 gm^{-3} only shifts the graph towards negative x-axis and similarly a reduction in maximum absolute temperature; the same peak in pressure side (blue curve) depicting the loss of heat of fusion can be observed in Test-3.

Effect of atmospheric temperature

Change in atmospheric temperature mainly affects the type of ice (dry or wet). To study the type of accreted ice, analysis is carried out using DU96 profile at two different operating conditions – (test 2); temp = −5 C° velocity: 77 ms^{-1} and (test 4); temp: −20 C° velocity: 70 ms^{-1}.

Analysis of Figure 8 shows that glaze ice with horned structure emerges in wet ice conditions, whereas dry conditions lead to the formation of rime ice. Since the atmospheric temperature for dry conditions (Test-4) was set to –20 C°, plots for mean temperature distribution in Figure 9 show negative temperature during initial 60 s, when a thin layer of ice appears. On the suction side and at LE, temperature drops abruptly after 90 s. During test-4, fine smooth and dense rime ice is formed when dry-ice conditions are implemented, in contrast to test-2. Tightly packed grains of hard-rime equally cover both the suction and pressure sides extending till 20%–25% of chord length. The formation of rime for dry icing can be further supported by numerical analysis as presented in Liu and Hu (2018), Gao et al. (2017) and Jin and Virk (2019). A significant difference between both the cases exists in the absolute average temperature and temperature difference curves; negative environment below –10°C is feasible for rime ice formation. DU96 no longer follows its normal temperature curve as previously observed during variation in LWC and AOA; rather it maintains a uniform difference among all AOI throughout the course of rime ice accretion.
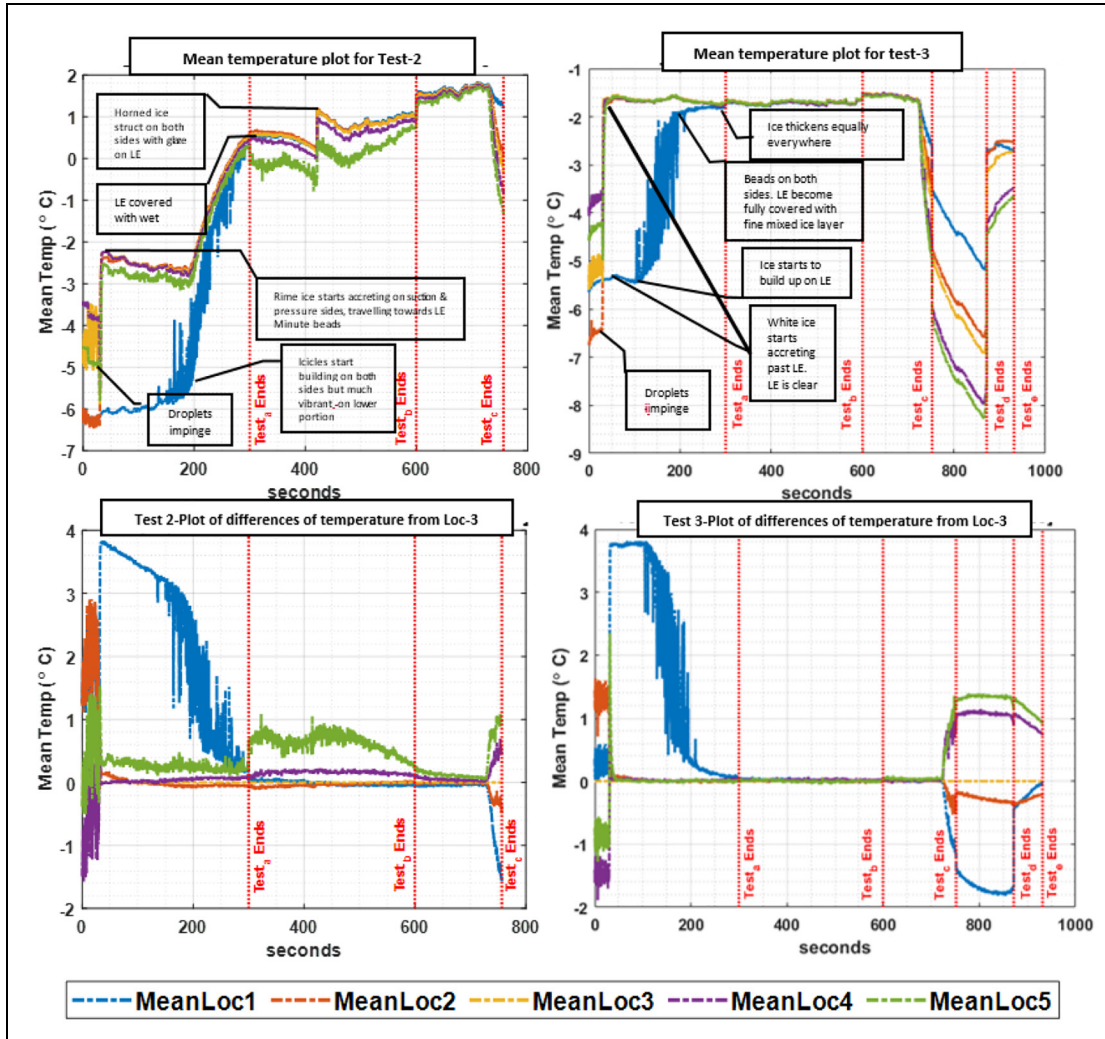
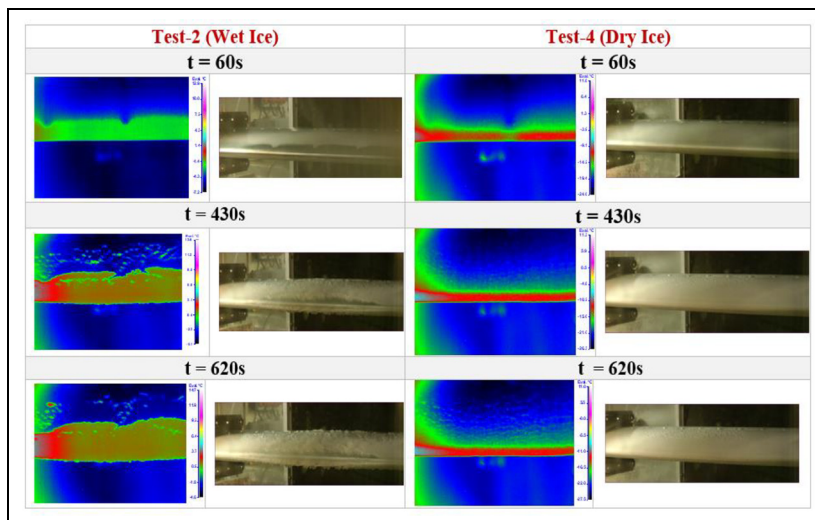**Figure 7.** Surface temperature variations during ice accretion – LWC case.

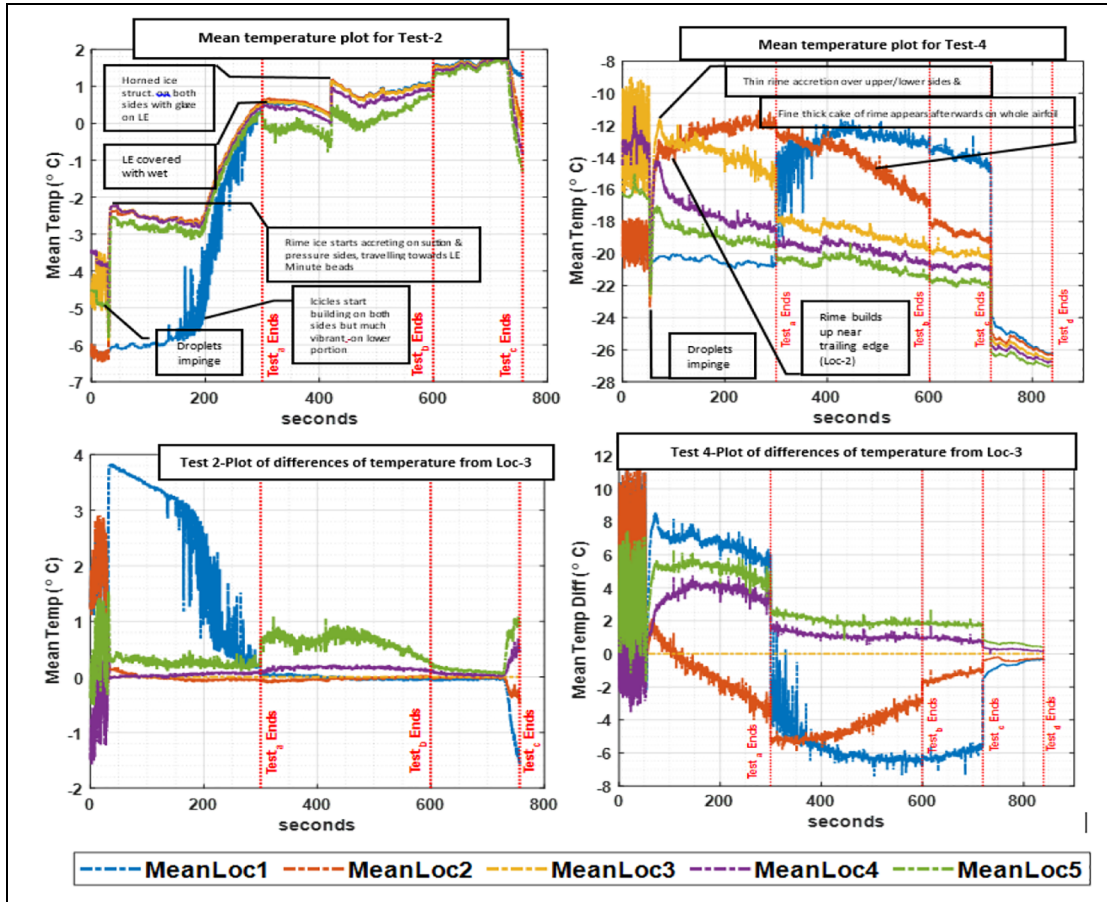**Figure 8.** Effect of atmospheric temperature variation.

Figure 9. Surface temperature variations during ice accretion – atmospheric temperature case.
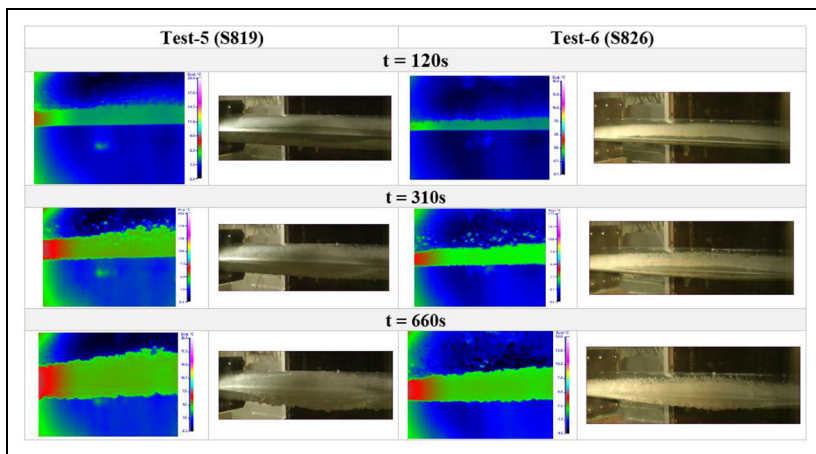

Figure 10. Effect of profile geometry on ice accretion – wet conditions.

Effect of profile geometry

Blade profile geometry affects the air flow and droplets behaviour that can lead to a change in ice accretion at same atmospheric conditions. To better understand the effect of blade profile geometry on surface temperature distribution and resultant ice accretion, detailed analyses are carried out for both dry and wet ice conditions.
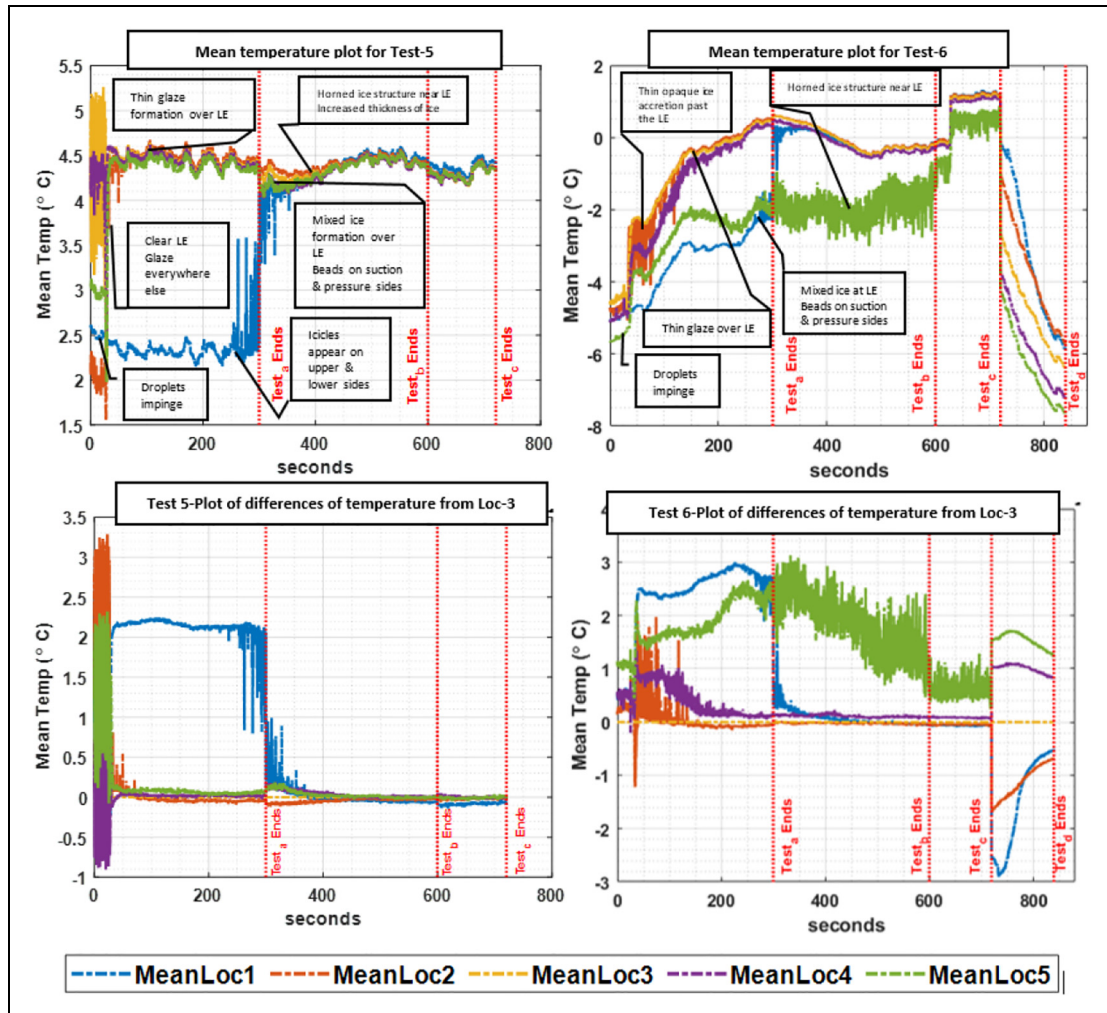
Figure .11 Profile geometry variations effect – wet conditions.
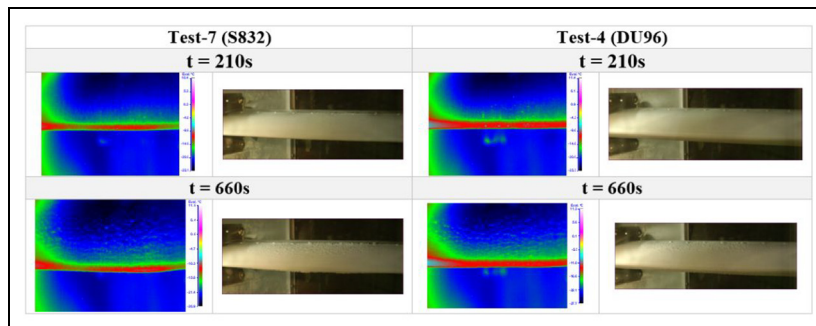

Figure 12. Effect of profile geometry on ice accretion – dry conditions.

Wet icing conditions. For wet ice conditions, analysis is carried out using S819 and S826 profiles (*tests 5* and *6*). Solid, smooth glaze ice is formed at stagnation line as well as towards the edges for S819 (Figure 10). Feathery spikes up to 10%–15% of chord length grow almost perpendicular to the normal of surface. Impingement of droplets first raises the temperature of the surface mainly due to the loss of heat of solidification/fusion to the environment. It can be observed in average temperature graphs at loc # 2, 3 and 4. However, horned ice structure
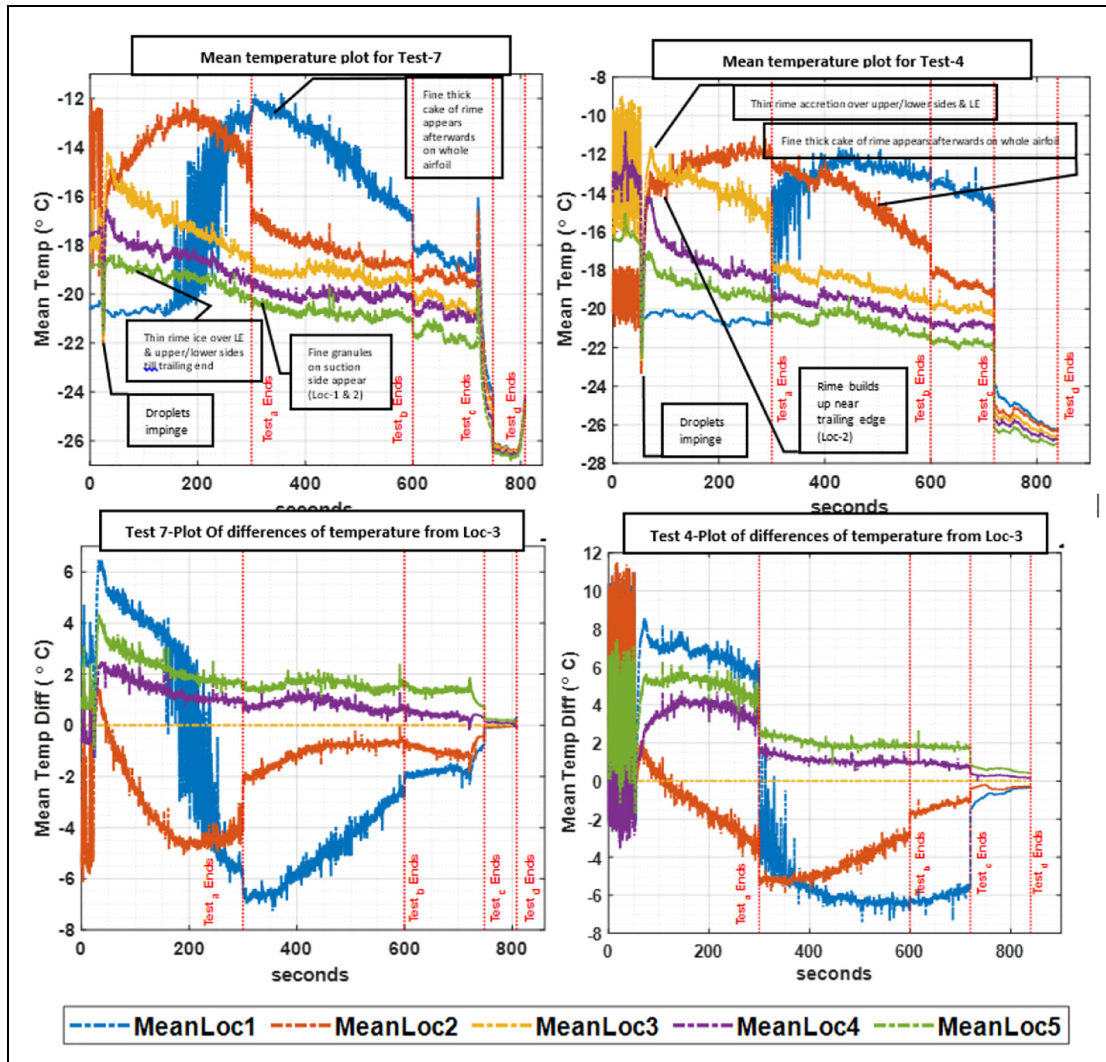
Figure 13. Profile geometry variations effect – dry conditions.

starts to build up past the LE first and then transcends to the LE. Almost equal height is achieved by ice accretion on suction and pressure sides.

For S826, wet glaze ice accreted at the stagnation line (Figure 10). On the top surface (suction side), ice deposit is around 5%–7% of the chord length and about 10% on pressure side. Along lower airfoil surface (pressure side), there is almost no ice accretion – a small amount extending from the main deposition at stagnation line (*approximately 2% of the chord length*) at the centre of the model, whereas towards the edges, the deposition and feathery glaze-like spike extend till approximately 10% of the chord length.

Thermal IR and HD camera images suggest that icing thickness is high in S819 as compared to S826 for the same time instant. Figure 11 depicts that initially ice deposition takes place in the form of flat solid glaze on both suction and pressure sides without accreting on LE and then at about 300s wet glaze starts appearing along the stagnation line in the form of feathery, glaze-like spikes. Another noticeable point is the positive absolute mean temperatures for S819.

Dry icing conditions. For dry icing conditions, analyses are carried out using S832 and DU96 profiles (*tests 4 and 7*). Fine layer of hard and dense ice accretion is obtained for both profiles (Figure 12). For S832 direction of the ice growth is parallel to the flow, which extends approximately 25% of the chord length on the top surface. On the bottom surface only beading is visible, extending approximately 10%–15% of the chord length in addition to the

beading past the first set of rivets, at approximately 30%–50% of the chord length (*rivets work as individual ice collectors*). For DU96 airfoil tightly packed rime ice grains along with nicely connected feathers extend till 20%–25% of chord length.

Graphical results in Figure 13 show that there is as no such prominent temperature difference between both the airfoils. Pressure side (blue and red curves) depicts a different behaviour, whereas other three curves for LE and suction side differ by approximately 1 C° only.

Conclusion

This preliminary study provided an insight of blade profile surface temperature distribution variation during ice accretion process at different operating and geometric conditions. Thermal IR image processing technique can be a useful way to study the ice accretion on wind turbine blade and design an optimum anti/de-icing strategy. Analysis shows that surface temperature distribution along blade profile surface during ice accretion process is a dynamic process and change in atmospheric conditions and blade geometric characteristics significantly effects the surface temperature and resultant ice accretion. The effect of blade geometry on ice accretion is more prominent in case of wet ice conditions due to low freezing fraction and water run back.

ORCID iD

Adeel Yousuf [iD] https://orcid.org/0000-0002-3311-6849

References

Afzal F and Virk MS (2018) Review of icing effects on wind turbine in cold regions. Available at: https://munin.uit.no/bitstream/handle/10037/14746/article.pdf?sequence=2&isAllowed=y

Gao L, Liu Y and Hu H (2017) An experimental investigation on the dynamic ice accretion process over the surface of a wind turbine blade model. In: *9th AIAA atmospheric and space environments conference*, Denver, CO, 5–9 June, pp. 707–718. Reston, VA: American Institute of Aeronautics and Astronautics.

Gao L, Liu Y and Hu H (2019) An experimental investigation of dynamic ice accretion process on a wind turbine airfoil model considering various icing conditions. *International Journal of Heat and Mass Transfer* 133: 930–939.

Ghani R and Virk MS (2013) Experimental study of atmospheric ice detection on wind turbine blade using thermal infrared technique. *Wind Engineering* 37(1): 71–77.

Gong X and Bansmer S (2015) 3-D ice shape measurements using mid-infrared LASER scanning. *Optics Express* 23: 4908–4926.

Guo H, Zhang K, Waldman R, et al. (2017) *An Experimental Study on Icing Physics for Wind Turbine Icing Mitigation*. Reston, VA: American Institute of Aeronautics and Astronautics.

Hudecz A (2014) *Icing Problems of Wind Turbine Blades in Cold Climates*. Lyngby: DTU Orbit; Denmark Technical University.

Jin JY and Virk MS (2019) Study of ice accretion and icing effects on aerodynamic characteristics of DU96 wind turbine blade profile. *Cold Regions Science and Technology* 160: 119–127.

Light J, Parthasarathy S and McIver W (2012) Monitoring winter ice conditions using thermal imaging cameras equipped with infrared microbolometer sensors. *Procedia Computer Science* 10: 1158–1165.

Liu Y and Hu H (2018) An experimental investigation on the unsteady heat transfer process over an ice accreting airfoil surface. *International Journal of Heat and Mass Transfer* 122: 707–718.

Meitzler T, Bryk D, Sohn E, et al. (2007) *MDA Ice Detection and Measurement Camera Development and Validation for NASA-KSC (2004-2007)*. Warren, MI: Visual Perception Laboratory (VPL); TARDEC; NASA.

Mohseni M, Frioult M and Amirfazli A (2012) Simultaneous monitoring of ice accretion and thermography of an airfoil: An IR imaging methodology. *Measurement Science and Technology* 23(10): 105405.

Rashid T, Khawaja HA and Edvardsen K (2019) Measuring thickness of marine ice using IR thermography. *Cold Regions Science and Technology* 128: 221–229.

Tammelin B, Böhringer A, Cavaliere M, et al. (2000) *Wind Energy Production in Cold Climate (WECO)*. Helsinki: Finnish Meteorological Institute.